International Journal of Thermal Sciences 102 (2016) 308–318

Contents lists available at ScienceDirect

International Journal of Thermal Sciences

journal homepage: www.elsevier.com/locate/ijts

Diffusion and separation mechanism of transient electromagnetic and thermal fields

Yizhe Wang [a], Bin Gao [a,*], Guiyun Tian [a,b], W.L. Woo [b], Yunqi Miao [a]

[a] School of Automation Engineering, University of Electronic Science and Technology of China, Chengdu, China
[b] School of Electrical and Electronic Engineering, Newcastle University, England, United Kingdom

ARTICLE INFO

Article history:
Received 26 August 2015
Received in revised form
27 October 2015
Accepted 16 November 2015
Available online xxx

Keywords:
Eddy current pulsed thermography
Joule heating
Thermal diffusion
Physical-mathematical model
Quantitative nondestructive testing and evaluation

ABSTRACT

Electromagnetic mechanism of Joule heating and thermal diffusion has considerable impacts on eddy current pulsed thermography (ECPT). Since ECPT is a multi-physics non-destructive testing (NDT) method depended on both transient electromagnetic and thermal fields, it is crucial to analyze the characteristic of heat propagation mechanism, characteristic time of diffusion as well as the separation of electromagnetic-thermal field for improving detection sensitivity and quantitative analysis. Deep inside to electromagnetic energy, this research constructs a physical-mathematical time-dependent partition model to analyze the whole thermal transient process and consider characteristic times for separating Joule heating and thermal diffusion into four different stage. This study sheds light not only on the deeper understanding of physical mechanism of inductive heating propagation but also on the better modeling and mining of mathematical time-spatial pattern in quantitative defects detection for NDT. Finally, numerical modeling and experiments have been conducted on both artificial slot of steel sample and natural edge crack on the turbine blade sample to validate the proposed study.

1. Introduction

Historically, temperature has been proved to be a pretty popular and significant indicator [1]. In 1934, Hardy [2,3] established the diagnostic importance of temperature measurement by using infrared thermography (IRT) in medical sciences. IRT is a nondestructive, nonintrusive, noncontact technique that captures the mapping of thermal patterns on the surface of objects, bodies or systems through an infrared imaging instrument [4]. Recently IRT has been successfully used not only in diseases diagnosis [5,6], such as breast tumor [7,8], but also in industry measurement, such as the thermography based nondestructive testing and evaluation due to its speed and ease of use and wide range of inspection [9].

Thermography is an attractive technique gaining popularity in NDT applications [10–16]. The outstanding advantage of thermography over other techniques is its potential in rapid inspection over a large area with high spatial resolution and sensitivity in a short period of time. However, there is a trade-off between detectable defect size and inspection area. Thermography is applicable to a wide range of materials, including composites and metallic materials, where specific excitation techniques are suitable for different applications. Thermography NDT method is generally divided into two main streams: passive infrared thermography (PIT) and active infrared thermography (AIT). PIT utilizes the natural temperature gap between the materials/structures and the ambient temperature. However, AIT requires an external excitation to generate a thermal contrast on the object surface, which is widely accepted that the active approach can be divided into optical, mechanical and inductive [17,18].

Optical thermography (OT) using photographic flashes or optical LT (lock-in thermography) halogen lamps is prevalence applied in the industrial inspection. However, the reflected heat from the material under inspection leads to the uneven heating on surface and cause unwanted interferes which results low signal to noise ratio (SNR) [17,19]. Ultrasound thermography (UT) [20–22] (also known as vibrothermography or thermosonics) could provide varying excitation waves (transverse wave [23], longitudinal wave [24] or guided wave [25]) for detection in accordance with diverse inspection requirements. However, the unreliability of contact between the test piece and the ultrasonic probe leads to highly instable in vibration spectrum which deteriorate the detectability of defect [26]. Inductive thermography (IT) [27,28] is a way of noncontact inspection. Based on electromagnetic induction principle,

* Corresponding author.
E-mail address: bin_gao@uestc.edu.cn (B. Gao).

http://dx.doi.org/10.1016/j.ijthermalsci.2015.11.016
1290-0729/

eddy currents are produced and then converted to Joule heating through ohmic loss. As eddy currents are generated in the conductor, it has the advantage of a high thermal efficiency and reduces the influence of external interference factors.

Eddy current pulsed thermography (ECPT) is an emerging inductive thermography [29–31] for detecting turbulence in conductive materials which combines the advantages of both pulsed eddy current and thermography testing [32]. A high-current pulse continued few milliseconds as an excitation signal drives to the coil which induces eddy current in the conductor. The transient surface temperature distribution from heat conduction (included Joule heating and heat diffusion) can be utilized to detect anomalies by analyzing the thermal patterns from infrared camera. The significant developments of ECPT technology have been applied in various industrial applications such as in aerospace [33], marine structure [34], power system [35], renewable energy [36] and rail [37]. The rich spatial-transient information of ECPT has attracted a wide range of interests. Yang et al. were extracted characteristic features from differential phase spectra to measure the defect's depth under different heating time using eddy current pulsed phase thermography (ECPPT) [38]. He et al. analyzed the detection and impact mechanism for carbon fiber reinforced plastic (CFRP) under reflection and transmission modes reflection and transmission modes [39]. Gao et al. characterized and tracked the different variation of physical properties in material using ECPT for Quantitative NDT&E [40]. Liu proposed the optical flow entropy tracking method to trace the heat flow and characterize the degree of fatigue damage [41]. Yang et al. introduced ECPPT for CFRPs evaluation considering volumetric induction heating due to small electrical conductivity, abnormal thermal wave propagation, and Fourier analysis [42]. Biju et al. determined the electrical and the thermal properties of a given isotropic material simultaneously from the time–temperature data from eddy current thermography [43].

All of the above researches recognize the basic physical mechanism corresponding to the general behavior of ECPT is the result of Joule heating via eddy current and thermal diffusion. The fundamental understanding of these two physical phenomena directly affects how to mine the optimal transient frame in feature extraction and pattern recognition for the quantitative defect analysis and characterization. John et al. [32] applied finite element method and experimental studies to understand the eddy current pulsed thermography. Yin et al. [44] explained the induction heating process and the patterns of resultant temperature distribution in different stages of ECPT by observing the experimental data. Yin considered the both initial process of heating phase and cooling phase continued 5 ms from the experimental data. However, these signal processing tools are not fully linked to the physics mechanism. While the results are acceptable but can be further developed to make it more accurate.

This paper establishes a derivation of time-dependent partition model to explain the physical mechanism of ECPT. A characteristic time period for the various stages rendered by the electromagnetic field is interpreted. In addition, the Joule heating via eddy current and heat diffusion decomposed by the heat conduction equation are discussed. Both numerical modeling and real experiment test have been conducted on an artificial slot of steel sample to validate the proposed study. The natural crack at the edge of the turbine blade is conducted as well. The effect of the different stages selection for quantitative surface defect analysis is reported.

The rest of this paper has been organized as follows. Firstly, a brief introduction of the ECPT system and a background theory are presented in Section 2. The physical-mathematical time-dependent partition model for stage interpretation and separation of ECPT is described in Section 3. Simulation and experiment of slot defect in the steel sample and the natural edge crack on the turbine blade as case studies have been used to validate the model. This is discussed in Section 4. Finally, conclusions and further work are outlined in Section 5.

2. Methodology

2.1. Introduction of ECPT system

Fig. 1 shows the schematic diagram of ECPT. The synchronized trigger device stimulates two pulse signals at the same time to control IR camera and induction heating element, respectively. These pulse signals, playing as switches, determine the excitation time. The excitation signal generated by the induction heating element perform high frequency current which continuing few milliseconds. It is driven to the transmitter coil above the conductor which will induce the eddy currents and generate the resistive heat in the conductive material. In addition, circulating cooling water through the coil is applied to eliminate the thermal radiation by the brass coil. The three-dimensional heat diffusion leads the flow from high to low temperature area, and then reduces the contrast till the heat balance in material. If a defect (e.g. crack, fatigue region) exists in conductive material, the distribution of eddy current or the process of thermal diffusion will be disturbance. Consequently, the resultant surface heat distribution and the transient thermal time-spatial response will show the variation captured by an infrared camera [40].

2.2. Background theory for ECPT

The main physical process of ECPT are involved by induced eddy currents heating and thermal diffusion. Heat conduction equation connects with electromagnetic and thermal fields.

2.2.1. Electromagnetic field

The differential Maxwell's equations form can be written as:

$$\nabla \times \mathrm{H} = \mathrm{J} + \frac{\partial \mathrm{D}}{\partial t} = \mathrm{J_s} + \mathrm{J_e} + \frac{\partial \mathrm{D}}{\partial t} \quad \text{(from Ampere's law)} \tag{1}$$

$$\nabla \times \mathrm{E} = -\frac{\partial \mathrm{B}}{\partial t} \quad \text{(from Faraday's law)} \tag{2}$$

where **H** is magnetic field intensity, **J** is the total charge current density, $\mathbf{J_s}$ is the external current density, $\mathbf{J_e}$ is the induced current density, **D** is the electric displacement vector, **E** is the electric field intensity, **B** is the magnetic flux density.

Constitutive equations in electromagnetism are given by:

$$\mathbf{D} = \varepsilon \mathbf{E} \tag{3}$$

$$\mathbf{J_e} = \sigma \mathbf{E} \tag{4}$$

$$\mathbf{B} = \mu \mathbf{H} \tag{5}$$

where ε is permittivity,σ is the electrical conductivity and μ is the magnetic permeability of the medium. The vector potential A is definition as:

$$\mathbf{B} = \nabla \times \mathbf{A} \tag{6}$$

and assuming axi-symmetric condition, we can transform Eqs. (1)–(6) into electromagnetic governing equation:

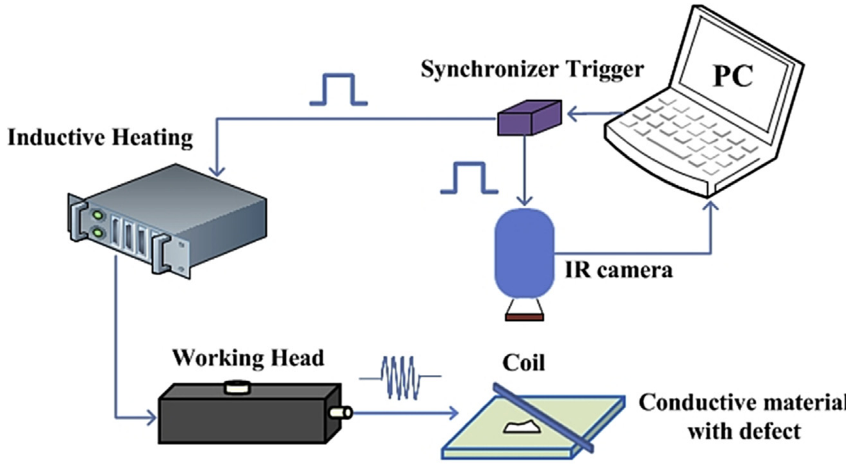

Fig. 1. ECPT schematic diagram.

$$\nabla \times \left(\frac{1}{\mu}\nabla \times \mathbf{A}\right) + \sigma\frac{\partial \mathbf{A}}{\partial t} + \varepsilon\frac{\partial^2 \mathbf{A}}{\partial t^2} = \mathbf{J_s} \tag{7}$$

The excitation frequency of ECPT is typically chosen from dozens to several hundred kHz. At this frequency electric displacement vector **D** can be ignored in the metallic material. Thus, the Eq. (7) can be written as:

$$\frac{1}{\mu}\nabla^2 \mathbf{A} + \sigma\frac{\partial \mathbf{A}}{\partial t} = \mathbf{J_s} \tag{8}$$

After setting the boundary conditions, the distribution of eddy currents induced in the conductor can be solved using the finite element method (FEM) through the Eq. (8). In a semi-infinite plane, eddy current density in depth direction meets the following conditions:

$$J_e(z) = J_e(0)\cdot e^{-z\sqrt{\pi\mu\sigma f}} \tag{9}$$

where z represents depth, and f is excitation frequency. $J_e(0)$ shows the surface eddy current density and it decays exponentially towards the interior of the conducting media, falling to $1/e$ of the value at the surface in a distance called the skin depth δ:

$$\delta = \frac{1}{\sqrt{\pi f \mu\sigma}} \tag{10}$$

2.2.2. Thermal field

The ECPT model is established according to multi-physics fields. The temperature of a conducting material will increase owing to resistive heating from the induced electric current. This is known as Joule heating which is the coupling of the electromagnetic and thermal fields.

According to Joule's Law:

$$Q = I^2Rt \tag{11}$$

where Q is the sum of the generated heat, I represents electric current, R is electrical resistance, and t is time. According to the definition of electrical resistance:

$$R = \frac{L}{\sigma S} \tag{12}$$

Where L is the Length of the conductor, S is the cross-sectional area of conductor. Since the relationship between the current and the induced current density J_e is:

$$I = J_e\cdot S \tag{13}$$

The Eqs. (12) and (13) is substituted into Eq. (11) to obtain Eq. (14):

$$Q = (J_e\cdot S)^2\cdot\frac{L}{\sigma S}\cdot t = \frac{1}{\sigma}|J_e|^2\cdot S\cdot L\cdot t = \frac{1}{\sigma}|J_e|^2\cdot V\cdot t \tag{14}$$

It is discussed in the unit volume per unit time. Therefore:

$$Q = \frac{1}{\sigma}|\,J_e\,|^2 \tag{15}$$

Also, the Eq. (4) is substituted into Eq. (15) to obtain Eq. (16):

$$Q = \frac{1}{\sigma}|\,J_e\,|^2 = \frac{1}{\sigma}|\sigma E|^2 \tag{16}$$

The above equation expresses the relationship between the sum of the generated heat Q, the induced current density J_e and electric field intensity E.

Since the energy conservation and Fourier heat conduction, inductive heat conduction equation can be expressed as:

$$\frac{\partial T}{\partial t} = \underbrace{\frac{\lambda}{\rho C_p}\left(\frac{\partial^2 T}{\partial x^2} + \frac{\partial^2 T}{\partial y^2} + \frac{\partial^2 T}{\partial z^2}\right)}_{\text{Thermal diffusion}} + \underbrace{\frac{1}{\rho C_p}q(x,y,z,t)}_{\text{Joule heating}} \tag{17}$$

where $T = T(x,y,z,t)$ is the transient surface temperature distribution, λ is the thermal conductivity of the material (W/m K), ρ is the density (kg/m^3), C_p is specific heat capacity (J/kg K), and $q(x,y,z,t)$ is the heat generation function per unit volume and unit time, which is the result of the Joule heating by eddy current. The heat conduction equation is merged with Joule heating and thermal diffusion.

In ECPT, defects cause disturbances on the electromagnetic and thermal fields will eventually be reflected on the surface transient temperature distribution. Due to the influence of three-dimensional thermal diffusion, it can detect deeper defects than electromagnetic NDT methods. Moreover, the ECPT has potential to characterize and track the properties variation of the material, such as electrical conductivity, magnetic permeability and thermal conductivity, for non-apparent defect such as fatigue and residual stress by establishing the links between the macroscopic properties and microscopic changes. Hence, it is necessary to do deep research on diffusion and separation of the transient electromagnetic and thermal fields for fundamental understanding of ECPT.

3. Physical-mathematical time-dependent partition model

For analyzing the diffusion characteristics and separation of heat conduction, it is necessary to build a physical-mathematical model. To derive the model, several premises are made: (1) all materials are isotropic, ferromagnetic and all properties do not change under different temperatures, (2) ideal pulse excitation signal, (3) satisfied Dirichlet boundary condition.

Induction heating consists of two phases: heating phase and cooling phase. In the heating phase, Joule heating and thermal diffusion co-exist. While in the cooling phase, only the thermal diffusion exists. Due to electromagnetic induction, the eddy current signals excited by the pulse rising and falling edges are equal whereas the directions are opposite [45]. The energy of the specimen obtained from the excitation source is invariant within the time of half pulse period. Thus, the time axis can be divided into several cycles which length equals to half pulse period and this is shown in Fig. 2. The total number of cycles (m) in heating phase can be expressed as:

$$m = \frac{T_{heat}}{T_{pulse}/2} = 2 \cdot T_{heat} \cdot f_{pulse} \tag{18}$$

where T_{heat} is the duration of heating phase. T_{pulse} and f_{pulse} represent pulse period and frequency, respectively. Suppose T represents cycle length and t_n represents the n-th cycle, namely:

$$t_n \in [(n-1)T, nT], n = 1, \cdots\cdots, m \tag{19}$$

When pulse signal is triggered, eddy current is induced in the sample. The mechanism by which the magnetic flux enters a material and then recovers to electro- and magneto-static equilibrium can be described as a three step process [46]: In the first step, free charges are expelled from the volume. The time for expulsion of free charges from the volume is negligible. For example, in Cu, it is approximately 10^{-19} s, far less than the collision time of 10^{-14} s [47]. In the second step, magnetic and electric fields are expelled. In the last step, the induced currents and electromagnetic fields are damped. Since the response of first step is significantly fast, the timescale to achieve equilibrium is dominated by the second and third steps. Relaxation timescale τ_D for expulsion out of and diffusion into the conducting volume was considered to be $10^{-4}s$ [47–49]. As an example, for copper (Cu), with a conductivity of $5.8 \times 10^7 (\Omega \cdot m)^{-1}$ and characteristic length of 1 mm, the diffusion time is $\tau_D = 7.3 \times 10^{-5}s$ [47]. Thus, in the time domain, transient electromagnetic responses could be generally expressed as a time-dependent exponential with relaxation time τ_D [48].

ECPT chooses high-frequency excitation to obtain better heating performance. However, high-frequency excitation causes an issue: cycle length T in time-dependent partition model is much shorter than the relaxation time of eddy currents τ_D, consequently the signals of eddy currents induced by different cycles overlap reciprocally and this is shown in Fig. 2.

Suppose that the zero-crossing time of the eddy current signal induced by the first pulse edge is τ_f, and assume $p = \tau_f/T$ which indicates the signal ends in the p-th cycle, then this signal can be segmented into p sections as:

$$U_1(t) = \sum_{i=1}^{p} u_{1i}(\mathrm{t}) \tag{20}$$

where $U_1(t)$ and $u_{1i}(t)$ represents total voltage response of first eddy current and the i-th section of this voltage response, respectively. Since the sample is not pure resistance, the impedance of sample Z can be expressed as follows:

$$Z = R + jX \tag{21}$$

where R denotes the equivalent resistance, and X denotes the equivalent reactance. Due to ohmic loss, part of the energy of induced eddy current is converted into heat. Let Q_{ki} be the generated resistive heat in the i-th cycle by the k-th eddy current signal, in which $k \in [1, m], i \in [k, k+p]$, this gives:

$$Q_{ki} = \int_{(i-1)T}^{iT} \frac{U_k^2(t)}{|Z|} \cdot dt \tag{22}$$

where $U_k(t)$ is the voltage response of the k-th eddy current signal. As the generated energy by the excitation source in each cycle is identical, namely

$$\Delta Q_0 = Q_k = \sum_i Q_{ki} \tag{23}$$

where ΔQ_0 and Q_k denote the generated resistive heat of each eddy current and the k-th eddy current, respectively.

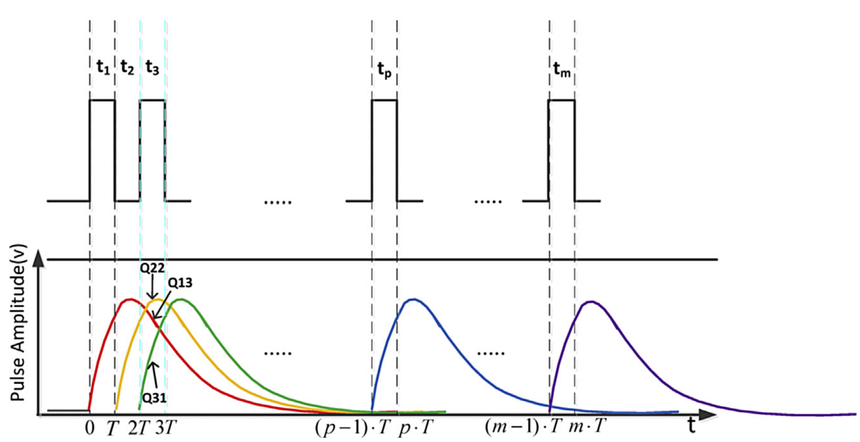

Fig. 2. Schematic diagram of physical-mathematical time-dependent partition model.

The energy of electromagnetic field is the bridge between the physical and mathematical derivation. Let E_n represent the sum energy of the generated resistive heat in the *n-th* cycle generated by different eddy current signals. Thus, the derivation and characteristic diffusion time of the four stages of inductive heating process will be given as:

Stage 1: If $1 \le n < p$, take $n = 3$ as an example and the energy of the *3-rd* cycle can be expressed as follow which is shown in Fig. 2:

$$E_3 = Q_{13} + Q_{22} + Q_{31} \tag{24}$$

Therefore,

$$E_n = \sum_{i=1}^{n} Q_{i(n-i+1)} \tag{25}$$

Note that E_n is a monotonically increasing function. According to the period range, Stage 1 represents the equilibrium process of electromagnetic field. Hence the characteristic diffusion time equals to relaxation timescale τ_D.

Stage 2: If $p \le n \le m$, take $n = p$ as an example and the energy of the *p-th* cycle can be expressed as follow:

$$E_p = Q_{p1} + Q_{(p-1)2} + \cdots\cdots + Q_{2(p-1)} + Q_{1p} \tag{26}$$

By this analysis, then E_n can be expressed as:

$$E_n = Q_{n1} + Q_{(n-1)2} + \cdots\cdots + Q_{(n-p+2)(p-1)} + Q_{(n-p+1)p} \tag{27}$$

As $Q_{ki} = Q_{ri}, k, r \in [1, m]$:

$$E_n = Q_{n1} + Q_{n2} + \cdots\cdots + Q_{n(p-1)} + Q_{np} = \sum_{i=1}^{p} Q_{ni} = \Delta Q_0 \tag{28}$$

In this stage, the generated resistive heat E_n is constant. The mark of characteristic time of Stage 2 is the end of heating phase at *m-th* cycle.

Stage 3: If $m + 1 \le n \le m + p$, take $n = m + 1$ as an example and the energy of the *(m + 1)-th* cycle can be expressed as follow:

$$\begin{aligned} E_{m+1} &= Q_{m2} + \cdots\cdots + Q_{(n-p+2)(p-1)} + Q_{(n-p+1)p} \\ &= \Delta Q_0 - Q_{(m-1)1} = \Delta Q_0 - Q_{11} \end{aligned} \tag{29}$$

and

$$E_n = \Delta Q_0 - \sum_{i=m+1}^{n} Q_{(i-m)(n-i+1)} \tag{30}$$

Indeed this stage is the inverse process of Stage 1 and can be represented by a monotonically decreasing function. Therefore, both Stage 1 and Stage 3 have the same characteristic time which is equivalent to relaxation timescale τ_D.

Stage 4: If $m + p + 1 \le n$, eddy current has been dissipated in the sample, namely:

$$E_n = 0 \tag{31}$$

The characteristic time of Stage 4 could be expressed by the end of cooling phase.

Above all, the generated resistive heat equations can be summarized as:

$$E_n = \begin{cases} \sum_{i=1}^{n} Q_{i(n-i+1)} & 1 \le n < p; \\ \Delta Q_0 & p \le n \le m; \\ \Delta Q_0 - \sum_{i=m+1}^{n} Q_{(i-m)(n-i+1)} & m + 1 \le n \le m + p; \\ 0 & m + p + 1 \le n; \end{cases} \tag{32}$$

According to Eq. (32), induction heating can be divided into four stages from the perspective of electromagnetic energy. The characteristic time of each stage is associated with the relaxation time of the material. Each stage is explained separately from the electromagnetic and thermal fields:

Stage 1: The electromagnetic (EM) field plays a dominant role in this stage. The diffusion of the EM field into the conductor is appeared after the abrupt application (the beginning of pulse excitation signal) of a magnetic field to the conducting surface. Eddy current density increases quickly from null to maximum in the sample. The sum energy of the generated resistive heat continuously increases by mutual overlap of eddy currents induced by different cycles. At this stage, the heat propagate presents the maximum change rate because of sudden variations in the electromagnetic field. However, due to the extremely short period of time, it did not produce an obvious temperature difference between the heating and non-heating area so that heating diffusion cannot afford a decisive role at this stage. Characteristic time exactly equals to the relaxation time τ_D. The duration of Stage 1 equals to the *p-th* cycle according to Eq. (32), which is equivalent to the diffusion time of the EM field.

Stage 2: Three-dimensional heat diffusion reinforcement plays a main role in Stage 2. Eddy current density and distribution maintain the steady state. The sum of the generated resistive heat E_n is constant. The temperature of the heating area gradually increased draws an obvious distinction to the non-heating area. According to Fourier's law of heat conduction, heat propagation gradually increases following this distinction. With the strengthening of thermal diffusion, the gradient of temperature declines while the temperature is still on the rise which leads to the decline of gradient of the thermal diffusion in turn. In addition, when gradient of temperature tends to constant, the increase tendency of thermal diffusion attains equilibrium state. Hence, the velocity variation of temperature remains unchanged due to the both stable states between thermal diffusion and eddy currents.

Stage 3: The cooling phase starts as excitation completed. This stage is the inverse process of Stage 1, in which characteristic time equals to the relaxation time τ_D. Eddy current density is quickly decreased from maximum to null in the sample. The sum energy of the generated resistive heat is continuously decreases over this period of time. At this stage, the change rate of thermal diffusion reaches the maximum whereas the value variation is negligible.

Stage 4: With the disappearance of the eddy current, only heat diffusion phenomena lefts. In this stage, the role of the thermal diffusion is very similar to Stage 2. As the temperature dropped, the thermal diffusion reduces, bringing a decrease in the gradient of the temperature, which in return contributes to the decline of the change rate of the thermal diffusion. Finally, the temperature of the conductor returns to the ambient temperature.

4. Validation of the model:Simulation and experimental

The above analysis divides the physical process into four stages and clearly presents the characteristic time of each stage. It summarizes the interpretation of physical mechanism through the separation of multi-physics field of ECPT. In order to validate the model, finite element model and real experiments are established.

4.1. Simulation and experimental set-up

An isotropic steel sample (ferrimagnet) contained a narrow, surface breaking slot in the middle and the natural edge crack on the turbine blade are used. The size of slot in steel is 30 mm*0.35 mm*6 mm (height*width*depth). A linear inductor is placed parallel to the upper plane of the sample, as shown in Fig. 3 (a), (c) and (d). The physical characteristics of the model to be studied are given on Table 1. The current input for the coil is set at 350 A with a frequency of 256 kHz. A 300 ms heating duration is selected for inspection, which is long enough to elicit an observable heat pattern, and 600 ms videos are recorded.

Numerical simulation was performed using COMSOL Multiphysics simulation software via the electro-thermal module which combines the application mode for induction currents and general heat transfer. The linear inductor was located at a position 5 mm away from the steel sample. The outer diameter of the coil is 3.5 mm and the inner diameter of the coil is 2.5 mm. In numerical simulation, the setting of parameters and geometry of excitation coil are fully consistent with the experiment. The experimental set-up of slot defect in the steel and the natural edge crack on the turbine blade are shown respectively in Fig. 3 (b) and (d). An Easyheat 224 from Cheltenham Induction Heating is used for excitation. Water cooling of coil is implemented to counteract thermal radiation from the coil. An SC7500 IR camera is a Stirling cooled camera with a 320 × 256 array of 1.5–5 μm InSb detectors. This camera has a sensitivity of <20 mK and a maximum full frame rate of 383 Hz, with the option to increase frame rate with windowing of the image. In this study, the frame rate is 2000 Hz with a 80 × 64 array.

Table 1
Electrical and thermal parameters for steel used in the simulation.

Parameters	Steel
Conductivity, σ(S/m)	4.0319×10^6
Relative permeability, μ	100
Temperature coefficient (k^{-1})	12.3×10^{-6}
Density, d (kg/m^3)	7850
Heat capacity, Cp (J/kg K)	475
Thermal conductivity, λ (W/m K)	44.5

4.2. Results and discussion

A. The separation of multi-physics field.

The surface heat distribution can be used to detect anomalies by analyzing the thermal response from infrared camera. Fig. 4 shows the temperature spatial distribution on the surface of material from the simulation and experiment, respectively. The definition of impact area is the surface transient temperature distribution caused by the defect. The size and shape of impact area are selected by human annotation. Because the emissivity of the sample is unknown, digital level (dl) is used to describe the temperature rather than Celsius degree (°C). For getting proper comparison of experiment and simulation results, the data are mapped to the range [0, 1] through the method of min–max normalization. The conversion function is shown as:

$$T^*_{xy} = \frac{T_{xy} - T_{min}}{T_{max} - T_{min}} \tag{33}$$

where T_{min} and T_{max} are the lowest and highest temperature of one pixel in the rectangular impact area showed in Fig. 4 through

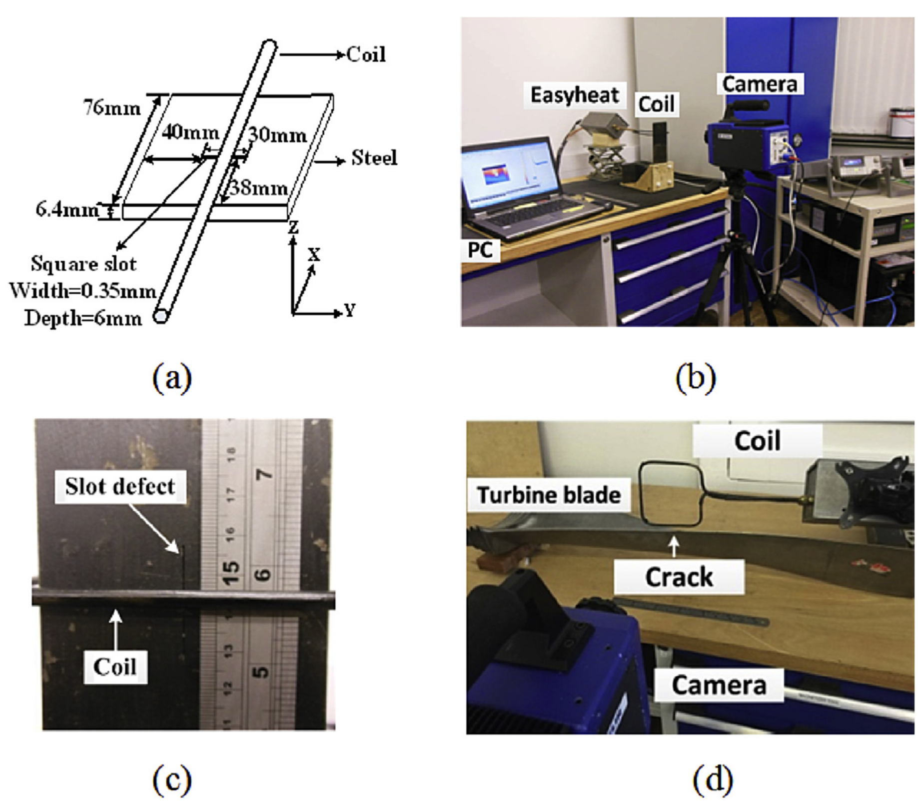

Fig. 3. (a) Finite element simulation model, (b) experimental setup, (c) steel sample with slot defect and (d) turbine blade with crack.

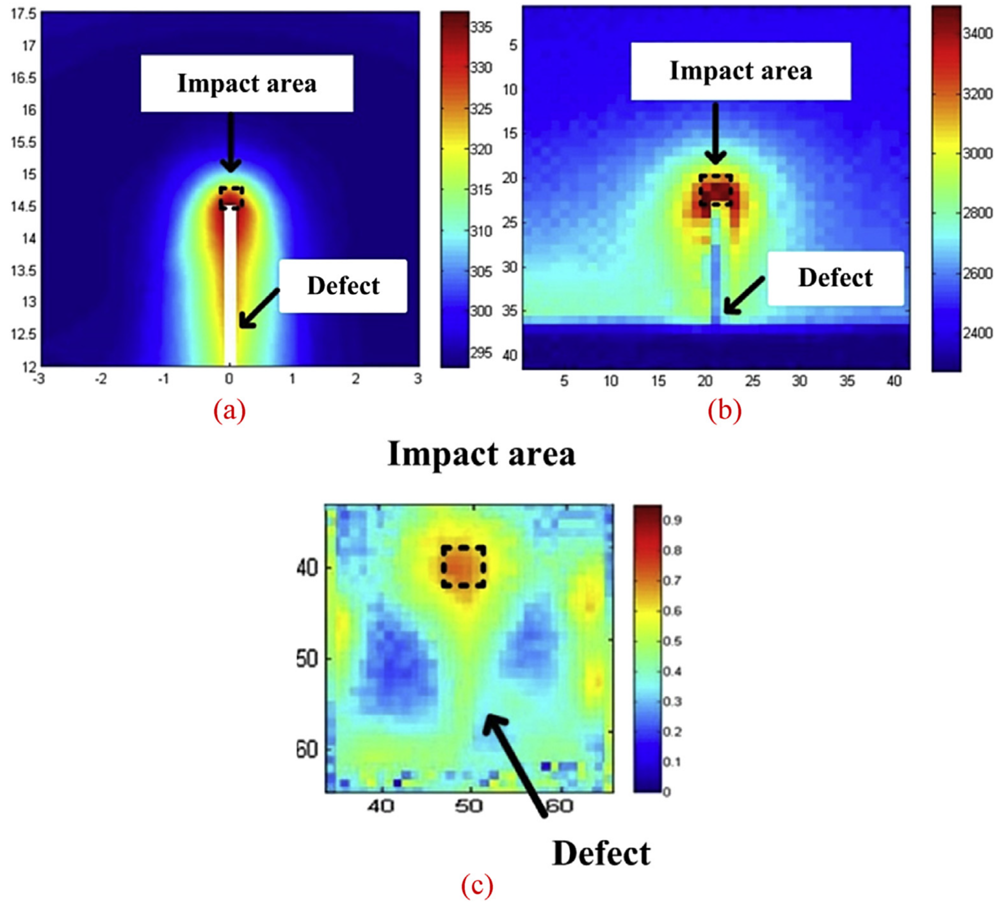

Fig. 4. (a), (b) and (c) the surface transient temperature distribution from the simulation, steel experiment and turbine blade testing respectively.

the whole ECPT video. T_{xy} denotes the temperature of this pixel in the impact area. T^{*}_{xy} is the normalized temperature of this pixel.

Figs. 5–7 reflect the physical field separation from the simulation and experiment results of slot defect in steel sample and the natural edge crack on the turbine blade, respectively. It is demonstrated the above explanation of each stage separated from the electromagnetic and thermal fields. Figs. 5–7(a) are the temperature profile which take the average of the temperature of all pixels in the impact area through the whole ECPT video. Figs. 5–7(b) show the first derivative of temperature against time dT/dt-t. According to Eq. (17), dT/dt can be decomposed into Joule heating generated by eddy current and thermal diffusion. According to Eq. (32), the curve of eddy current energy could be depicted so that thermal diffusion can be derived by removing the eddy current part from the superimposed curve. Figs. 5–7(c) show the separation of these two physical phenomena. During the heating and cooling phases, the curve of thermal diffusion is rotationally symmetrical. In Stage 1 and 3, the eddy current density is mutated which gives rise to the maximum slop of thermal diffusion. As the eddy current stabilizes in Stage 2 and 4, the tendency of the thermal diffusion is gradually leveled off. The variation in the thermal diffusion is concordant in heating and cooling phases. Figs. 5–7(c) also show the four separated stages. In order to validate our model, arbitrary selection of four frames from each relevant stage are explored to interpret the physical mechanism and used for discussing the impacts in quantitative defect evaluation.

B. Physical mechanism interpretation and quantitative defect evaluation for various stages.

Simulation and experimental results for different stages are presented in Fig. 8. According to Eq. (32), The duration of Stage 1 equals to *p-th* cycles in time-dependent partition model, which initializes the inductive heating and is coincidentally equivalent to relaxation time of eddy current τ_D ($0\sim10^{-4}$)s where the frame image of 0.5 ms is chosen as a candidate as shown in Fig. 2. When the eddy current encounters a discontinuity slot defect, it will be forced to divert, leading to the increase and decrease areas of eddy current density [6]. Hot spots are observed around the slot tips and the cool areas are located at the slot flanks. In this stage, the eddy current density quickly rises while heat diffusion does not play an obvious role due to the short duration. The time range of Stage 2 is $10^{-4}\sim0.3$s because the duration of Stage 1 is equivalent to 10^{-4} and the heating phase is set as 300 ms in the simulation and experiment. It is chosen the frame image of 10 ms, which is the random frame in this range, to represent Stage 2. The energy of the specimen obtained from the excitation source is ceaseless overlaid so that the temperature of specimen gradually rises. In addition, three-dimensional heat diffusion reinforcement plays a major role in this stage. As shown in Fig. 8, the thermal diffusion of Stage 2 is significantly more intense than Stage 1. When the excitation completed, Stage 3 begins which is also the starting of the cooling phase. This stage is the inverse process of Stage 1, which has the same relaxation time τ_D. Therefore, the frame image at 300.5 ms is selected. The excitation signal stopped which causes the eddy current disappear rapidly. Finally, the frame image 500 ms is selected to characterize Stage 4 while eddy current disappears and only heat diffusion process exists which leads the flow from high to low temperature area, and then reduces the contrast which makes

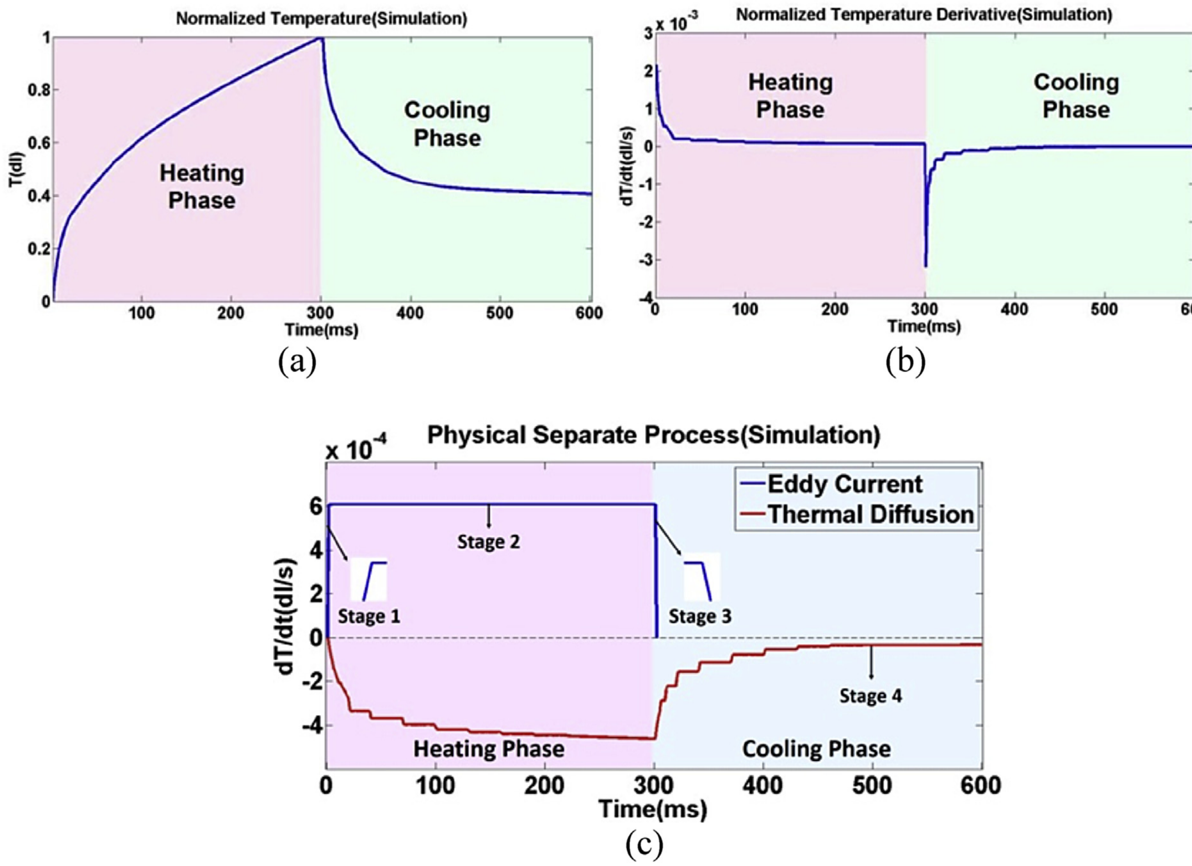

Fig. 5. Simulation results: (a) transient temperature response at impact area against time, (b) 1st derivatives of temperature response, and (c) physical separation of eddy current and thermal diffusion.

the entire image blurred in Fig. 8. In this stage, it has been difficult to obtain quantitative information of the defect. Both numerical modeling and real experimental results have successfully verified the physical interpretation of the four stages.

In particular, the results show that the initial heating phase (Stage 1) can be considered the suitable time range for quantitative surface defect analysis as shown in Fig. 8. The width error is defined as the difference between the width of real defect and impact area. In numerical modeling of slot defect in the steel, the error rate of Stage 1 is $\alpha_1 = 14.3\%$. Compared with the error rate of the remaining stages, it improves 85.7%, 385.7% and 485.7%, respectively. In the corresponding experiment, the error rate of Stage 1 is $\beta_1 = 33.3\%$. Compared to the subsequent stages, it improves 100.3%, 266.7% and 500%, respectively. Because of the complex geometry, the results of natural edge crack on the turbine blade are not perfect compare with the simulation where the error rate of Stage 1 is $\gamma_1 = 40\%$. Compared to the subsequent stages, it improves 116%, 285% and 360%, respectively. The reason why Stage 1 has a good performance on quantitative analysis of defect is that ferromagnetic material has shallow skin depth and eddy current is intensive on the surface and circumambulates the defect tightly [50]. In Stage 1, the electromagnetic field distribution has been determined. At the same time, the lateral thermal diffusion has small effect on defect detection, which causes the blur of thermal images in subsequent stages. Finally, the thermal distribution can represent the eddy current field, and characterize the quantitative information of defects.

In this paper, case studies from simulation to natural crack have been conducted to evaluate the derivation of characteristic diffusion time, the physical interpretation and separation of the four stages of inductive heating. Not with standing above, it interprets different stages of ECPT which alternate distinct physical process. For different materials and structures, the chosen of appropriate stage (frame) will facilitate the defects detection as well as benefit the quantization analysis [51]. In addition, as a reminder, the method that subtracted image of the first frame in order to subtract the background noise may lose valuable quantitative information of defect.

5. Conclusion

This research establishes the link between physical mechanism and mathematical interpretation by the way of electromagnetic energy, and then constructs time-dependent partition model. Through this model, it divides the whole thermal transient process into four stages and reports the physical interpretation. A characteristic time for various stages by the electromagnetic field is presented. Two physical phenomena (Joule heating and thermal diffusion) in ECPT are separated to understand the basic mechanism. In the future, this fundamental understanding of division stages and characteristic times will be applied to the development of feature extraction and pattern recognition for the quantitative analysis of defects for ECPT.

An artificial slot of steel sample with both numerical modeling and experimental test as well as the natural edge crack on the turbine blade are conducted to validate the study. By extracting the temperature of impact area, the transient temperature response at impact area against time and the corresponding 1st derivatives of temperature response are obtained. These results (Figs. 5–7(c))

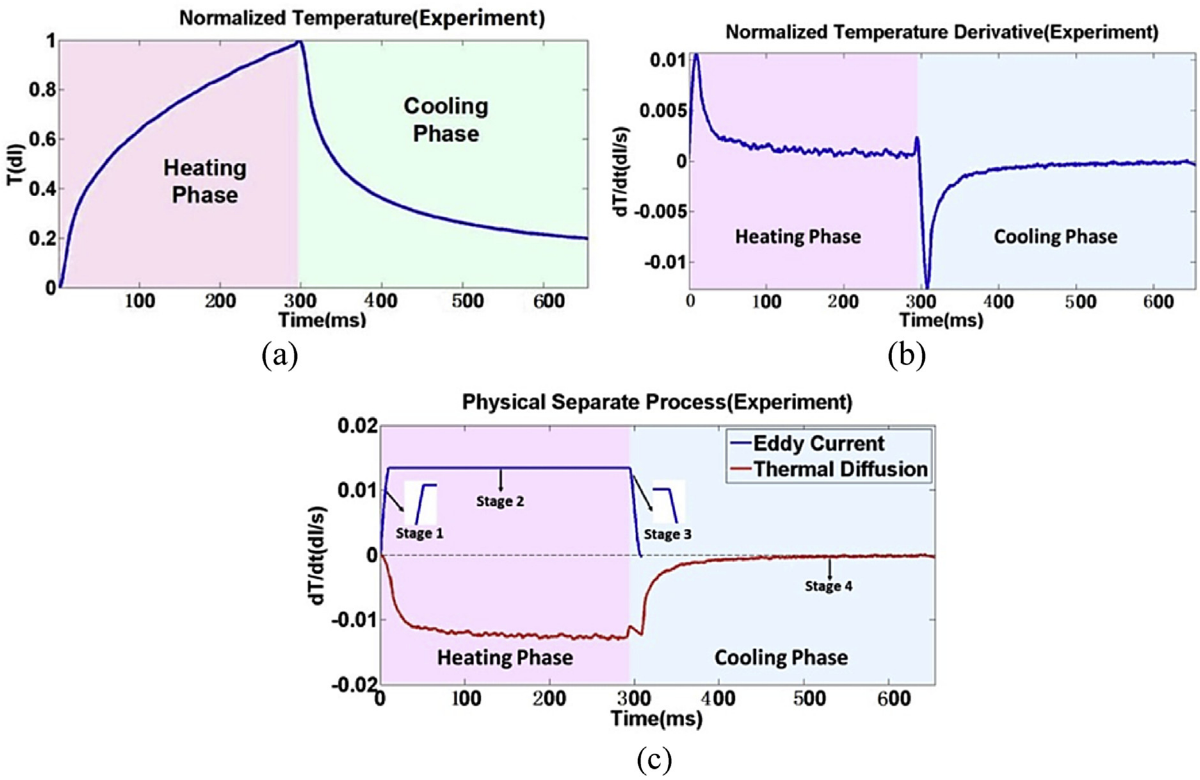

Fig. 6. Steel experimental results: (a) transient temperature response at impact area against time, (b) 1st derivatives of temperature response, and (c) physical separation of eddy current and thermal diffusion.

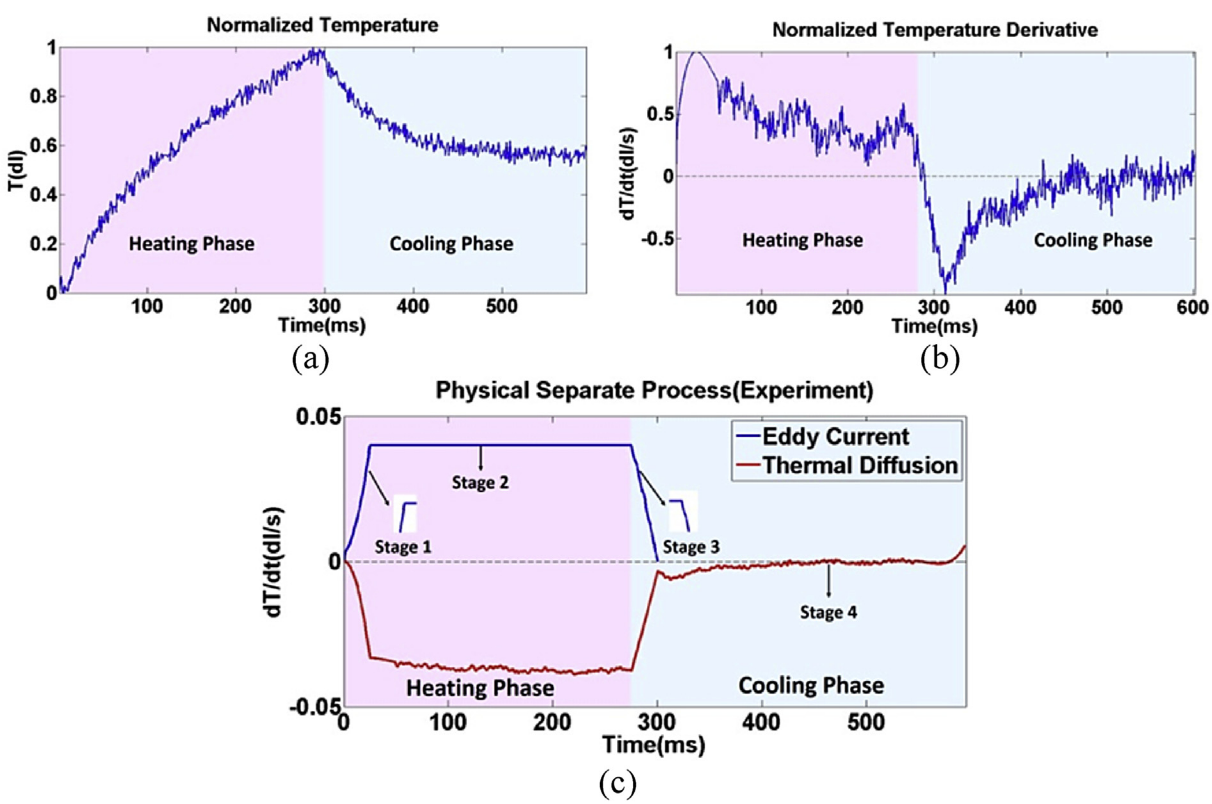

Fig. 7. Turbine blade testing results: (a) transient temperature response at impact area against time, (b) 1st derivatives of temperature response, and (c) physical separation of eddy current and thermal diffusion.

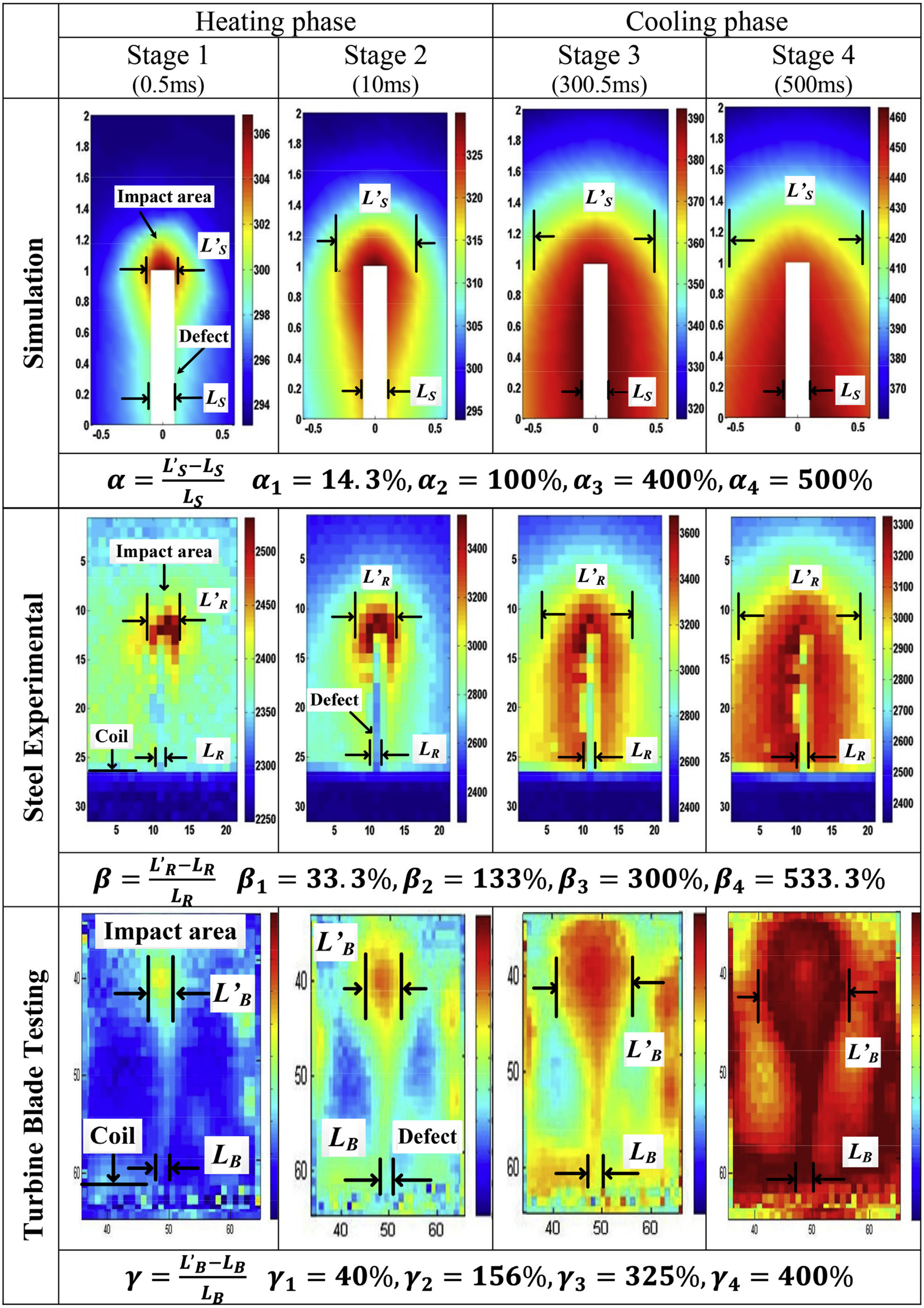

Fig. 8. Simulation, steel experimental and turbine blade results for different stages of induction heating.

show that this study not only is a suitable match to the stage mechanism of induction heating, but also show the effects of stages selection for quantitative analysis on surface defect.

Future work will focus on applying different physical transient stages and behaviors to further study the defect detection, such as cracking in turbine blades and impact damage in carbon fiber structures, and optimize the excitation parameters.

Acknowledgements

The work was supported by National Natural Science Foundation of China (Grant No. 51377015, No. 61401071 and No. 61527803), Supported by NSAF (Grant No. U1430115), FP7 HEMOW IRSES project 269202, China Postdoctoral Science Foundation (No.136413), the Science & Technology Department of Sichuan Province, China (Grant No. 2013HH0059), and the Fundamental Research Funds for the Central Universities (Grant No. ZYGX2014J068).

References

[1] E. Ring, The historical development of temperature measurement in medicine, Infrared Phys. Techn 49 (2007) 297–301.
[2] J.D. Hardy, The radiation of heat from the human body: III. The human skin as a black-body radiator, J. Clin. Invest 13 (1934) 615.
[3] J.D. Hardy, C. Muschenheim, Radiation of heat from the human body. V. The transmission of infra-red radiation through skin, J. Clin. Invest 15 (1936) 1.
[4] C. Ibarra-Castanedo, X.P. Maldague, in: H. Czichos (Ed.), Infrared Thermography Handbook of Technical Diagnostics: Fundamentals and Application to Structures and Systems, Springer, Berlin, 2013, pp. 175–220.
[5] B.B. Lahiri, S. Bagavathiappan, T. Jayakumar, J. Philip, Medical applications of infrared thermography: a review, Infrared Phys. Techns 55 (2012) 221–235.
[6] B.F. Jones, A reappraisal of the use of infrared thermal image analysis in medicine, Med. Imaging, IEEE Trans. 17 (6) (1998) 1019–1027.
[7] K.M. Lovett, B.A. Liang, Risks of online advertisement of direct-to-consumer thermography for breast cancer screening, Nat. Rev. Cancer 11 (2011) 827–828.
[8] E.Y.K. Ng, A review of thermography as promising non-invasive detection modality for breast tumor, Int. J. Therm. Sci. 48 (5) (2009) 849–859.
[9] C. Ibarra-Castanedo, J.R. Tarpani, X.P. Maldague, Nondestructive testing with thermography, Eur. J. Phys. 34 (2013) S91.
[10] S. Bagavathiappan, B.B. Lahiri, T. Saravanan, et al., Infrared thermography for condition monitoring—a review, Infrared Phys. Technol. 60 (2013) 35–55.
[11] R. Gade, T.B. Moeslund, Thermal cameras and applications: a survey, Mach. Vis. Appl. 25 (1) (2014) 245–262.
[12] P. Laloue, C. Bissieux, J.-F. Henry, H. Pron, J. L'Ecolier, F. Nigon, Infrared nondestructive measurement of thermal resistance between liner and engine block: design of experiment, Int. J. Therm. Sci. 47 (3) (2008), 249e260.
[13] Yong-Kai Zhu, Gui-Yun Tian, Rong-Sheng Lu, Hong Zhang, A review of optical NDT technologies, Sensors 11 (8) (8 August 2011), 7773e7798.
[14] Y.Y. Hung, Y.S. Chen, S.P. Ng, L. Liu, Y.H. Huang, B.L. Luk, R.W.L. Ip, C.M.L. Wu, P.S. Chung, Review and comparison of shearography and active thermography for nondestructive evaluation, Mater. Sci. Eng. 64 (5e6) (1 May 2009), 73e112.
[15] X. Maldague, Introduction to NDT by active infrared thermography, J. Mater. Eval 60 (9) (2002) 1060–1073.
[16] K. Miya, Recent advancement of electromagnetic nondestructive inspection technology in Japan, IEEE Trans. Magn. 38 (2) (2002) 321–326.
[17] Ph Menner, C. Spiessberger, A. Gleiter, G. Busse, Aerospace applications of lock in thermography with optical, ultrasonic and inductive excitation, AIP Conf. Proc. 1211 (5) (2010) 25–32.
[18] C. Ibarra-Castanedo, M. Genest, J.-M. Piau, S. Guibert, A. Bendada, X.P.V. Maldague, in: C.H. Chen (Ed.), Chapter 16: Active Infrared Thermography Techniques for the Nondestructive Testing of Materials Ultrasonic and Advanced Methods for Nondestructive Testing and Material Characterization, World Scientific, Singapore, 2007, p. 684.
[19] R. Montanini, F. Freni, Non-destructive evaluation of thick glass fiber-reinforced composites by means of optically excited lock-in thermography, Compos. A 43 (2012) 2075–2082.
[20] L.D. Favro, X. Han, Z. Ouyang, G. Sun, H. Sui, R.L. Thomas, Infrared imaging of defects heated by a sonic pulse, Rev. Sci. Instrum. 71 (2000) 2418–2421.
[21] S.M. Shepard, T. Ahmed, J.R. Lhota, Experimental considerations in vibro-thermography, Proc. SPIE 5405 (2004) 332–335.
[22] T. Zweschper, G. Riegert, A. Dillenz, G. Busse, Ultrasound excited thermography-advances due to frequency modulated elastic waves, J. Quant. Infrared Thermogr. 2 (2005) 65–76.
[23] Thompson J G, Uyehara C T. Ultrasonic thermography inspection method and apparatus: U.S. Patent 7,075,084[P]. 2006-7–11.
[24] S.D. Holland, C. Uhl, Z. Ouyang, et al., Quantifying the vibrothermographic effect, NDT E Int. 44 (8) (2011) 775–782.
[25] M. Rheinfurth, F. Schmidt, D. Döring, et al., Air-coupled guided waves combined with thermography for monitoring fatigue in biaxially loaded composite tubes, Compos. Sci. Technol. 71 (5) (2011) 600–608.
[26] M. Morbidini, P. Cawley, M.J.S. Lowe, T. Barden, D.P. Almond, A Quantitative Investigation of Thermosonics, WCNDT, Montreal, Canada, 2004.
[27] G. Riegert, T. Zweschper, G. Busse, Lock-in thermography with eddy-current excitation, J. Quant. Infrared Thermogr. 1 (2004) 21–32.
[28] M. Grenier, C. Ibarra-Castanedo, F. Luneau, BendadaHand MaldagueX2009 development of a field concentrator coil by finite element modeling for power efficiency optimization in eddy current thermography inspection review of quantitative nondestructive evaluation, in: AIP Conf. Proc., vol. 29, July 2009, pp. 361–368. Kingston, 1211ed D O Thompson and D E Chimenti.
[29] K. Leppänen, J. Saarela, R. Myllylä, T. Fabritius, Electrical heating synchronized with IR imaging to determine thin film defects, Opt. EXPRESS 21 (2013) 32358–32370.
[30] G. Tian, X. Zhou, A.D. Ibukun, Pulsed electromagnetic non-destructive evaluation and applications, Instrumentation 1 (2014) 3.
[31] F. Fertig, J. Greulich, S. Rein, Spatially resolved determination of the short-circuit current density of silicon solar cells via lock-in thermography, Appl. Phys. Lett. 104 (2014) 201111.
[32] J. Wilson, G.Y. Tian, I.Z. Abidin, S. Yang, D. Almond, Modeling and evaluation of eddy current stimulated thermography, Nondestruct Test. Eva 25 (2010) 205–218.
[33] L. Cheng, G.Y. Tian, Surface crack detection for carbon fiber reinforced plastic (CFRP) materials using pulsed eddy current thermography, Sensors J. IEEE 11 (2011) 3261–3268.
[34] G.Y. Tian, Y. He, L. Cheng, P. Jackson, Pulsed eddy current thermography for corrosion characterisation, Int. J. Appl. Electrom 39 (2012) 269–276.
[35] K. Li, G.Y. Tian, L. Cheng, A. Yin, W. Cao, S. Crichton, State detection of bond wires in IGBT modules using eddy current pulsed thermography, Power Electron. IEEE Trans. 29 (2014) 5000–5009.
[36] R. Yang, Eddy current volume heating thermography and phase analysis for imaging characterization of interface delamination in CFRP, IEEE Trans. Industrial Inf. PP (2015) 1.
[37] R. Yang, Y. He, B. Gao, et al., Lateral heat conduction based eddy current thermography for detection of parallel cracks and rail tread oblique cracks, Measurement 66 (2015) 54–61.
[38] Y. He, M. Pan, G.Y. Tian, et al., Eddy current pulsed phase thermography for subsurface defect quantitatively evaluation, Appl. Phys. Lett. 103 (14) (2013) 144108.
[39] Y. He, G. Tian, M. Pan, et al., Impact evaluation in carbon fiber reinforced plastic (CFRP) laminates using eddy current pulsed thermography, Compos. Struct. 109 (2014) 1–7.
[40] B. Gao, A. Yin, G. Tian, et al., Thermography spatial-transient-stage mathematical tensor construction and material property variation track, Int. J. Therm. Sci. 85 (2014) 112–122.
[41] J. Liu, Wenwei Ren, et al., Nondestructive evaluation of early contact fatigue using eddy current pulsed thermography, IEEE Sensors J. 15 (8) (AUGUST 2015).
[42] R. Yang, Y. He, Eddy current pulsed phase thermography considering volumetric induction heating for delamination evaluation in carbon fiber reinforced polymers, Appl. Phys. Lett. 106 (23) (2015) 234103.
[43] N. Biju, N. Ganesan, C.V. Krishnamurthy, K. Balasubramaniam, Simultaneous estimation of electrical and thermal properties of isotropic material from the tone-burst eddy current thermography (TBET) time–temperature data, IEEE Trans. Magn. 47 (2011) 2213–2219.
[44] A. Yin, B. Gao, G. Yun Tian, W.L. Woo, K. Li, Physical interpretation and separation of eddy current pulsed thermography, J. Appl. Phys. 113 (2013) 64101.
[45] D.J. Griffiths, Introduction to Electrodynamics, third ed., Prentice-Hall, Upper Saddle River, New Jersey, 1999, pp. 315–393.
[46] H.C. Ohanian, On the approach to electro-and magneto-static equilibrium, Am. J. Phys. 51 (1983) 1020–1022.
[47] N. Ashby, Relaxation of charge imbalances in conductors, Am. J. Phys. 43 (6) (1975) 553–555.
[48] T.W. Krause, C. Mandache, J. Lefebvre, Diffusion of pulsed eddy currents in thin conducting plates, in: Review of progress in quantitative nondestructive evaluation: 34th Annual Review of Progress in Quantitative Nondestructive Evaluation, AIP Publishing, 2008, pp. 368–375.
[49] C.S. Angani, D.G. Park, C.G. Kim, P. Leela, M. Kishore, Y.M. Cheong, Pulsed eddy current differential probe to detect the defects in a stainless steel pipe, J. Appl. Phys. 109 (2011) 7D–348D.
[50] B. Oswald-Tranta, Thermo-inductive crack detection, Nondestruct Test. Eva 22 (2007) 137–153.
[51] Bin Gao, Wai Woo, Yunze He, Gui Tian. Unsupervised sparse pattern diagnostic of defects with inductive thermography imaging system. IEEE Trans. Ind. Inform. (in press).